

Water/Ionic Liquid/Succinonitrile Hybrid Electrolytes for Aqueous Batteries

David Reber, Oleg Borodin, Maximilian Becker, Daniel Rentsch, Johannes Helmut Thienenkamp, Rabeb Grissa, Wengao Zhao, Abdessalem Aribia, Gunther Brunklaus, Corsin Battaglia, and Ruben-Simon Kühnel*

The water-in-salt concept has significantly improved the electrochemical stability of aqueous electrolytes, and the hybridization with organic solvents or ionic liquids has further enhanced their reductive stability, enabling cell chemistries with up to 150 Wh kg⁻¹ of active material. Here, a large design space is opened by introducing succinonitrile as a cosolvent in water/ionic liquid/succinonitrile hybrid electrolytes (WISHEs). By means of succinonitrile addition, the solubility limits can be fully circumvented, and the properties of the electrolytes can be optimized for various metrics such as highest electrochemical stability, maximum conductivity, or lowest cost. While excessive nitrile fractions render the mixtures flammable, careful selection of component ratios yields highly performant, nonflammable electrolytes that enable stable cycling of Li₄Ti₅O₁₂-LiNi_{0.8}Mn_{0.1}Co_{0.1}O₂ full cells over a wide temperature range with strong rate performance, facilitated by the fast conformational dynamics of succinonitrile. The WISHEs allow stable cycling with a maximum energy density of ≈140 Wh kg⁻¹ of active material, Coulombic efficiencies of close to 99.5% at 1C, and a capacity retention of 53% at 10C relative to 1C.

D. Reber, M. Becker, D. Rentsch, R. Grissa, W. Zhao, A. Aribia, C. Battaglia, R.-S. Kühnel Empa

Swiss Federal Laboratories for Materials Science and Technology 8600 Dübendorf, Switzerland

E-mail: ruben-simon.kuehnel@empa.ch

O. Borodin
Battery Science Branch
Energy Science Division
Sensors and Electron Devices Directorate
U.S. Army Research Laboratory
Adelphi, MD 20783, USA
M. Becker, A. Aribia
ETH Zurich
Department of Materials
8093 Zurich, Switzerland
J. H. Thienenkamp, G. Brunklaus
Helmholtz-Institute Münster
IEK-12
Forschungszentrum Jülich GmbH

The ORCID identification number(s) for the author(s) of this article can be found under https://doi.org/10.1002/adfm.202112138.

© 2022 The Authors. Advanced Functional Materials published by Wiley-VCH GmbH. This is an open access article under the terms of the Creative Commons Attribution License, which permits use, distribution and reproduction in any medium, provided the original work is properly cited.

DOI: 10.1002/adfm.202112138

48149 Münster, Germany

1. Introduction

The exploitation of highly concentrated electrolytes has significantly contributed to the development of aqueous batteries with improved cycling stability and increased operating voltage.[1-3] Driven by their nonflammability, straightforward assembly, and potential cost advantages, significant efforts have been invested extending the intrinsically towards narrow electrochemical stability window of water. Several aqueous batteries with energy densities of up to 150 Wh kg⁻¹ on the active material level, competitive to some nonaqueous chemistries, were introduced recently.[4-7] Archetypal waterin-salt (WiS) electrolytes are based on perfluorinated sulfonylimide salts such as lithium bis(trifluoromethanesulfonyl) imide (TFSI), where typically molalities >20 mol of salt per kg of water are

used (hereafter denoted as 20m), offering voltage windows of >2.5 V.[1-3,6,8-12] In contrast, dilute electrolytes typically do not withstand voltages above 1.5 V. With increasing salt concentration, more water molecules are incorporated into cation solvation shells and separated into clusters comprised of merely a few molecules. The strong coordination to cations and reduced water mobility results in kinetic overpotentials towards water electrolysis and formation of nanoscale percolation networks of anion- and water-rich domains that facilitate cation transport.[13,14] Furthermore, anions also strongly interact with the, typically alkali, cations at such high concentrations, facilitating the formation of anion-derived solid-electrolyte interphases (SEI), $^{[1,2,14-16]}$ highly dependent on the actual nature of the anions.[17] The exact mechanistic details of this SEI formation, likely direct electrochemical reduction^[1,2,15,18] or nucleophilic attack of hydroxide ions that form during initially extensive water reduction [19], is actively debated in current literature, and a superposition of both mechanisms appears likely to occur in practice. In WiS electrolytes, the oxidative stability is particularly improved due to the accumulation of bulky anions (e.g., TFSI) on the positive electrode and subsequent formation of a water exclusion zone. [20,21] Other attempts to increase the salt concentration to further push the overpotentials towards water reduction yet had limited success, since solubility limits restrict the maximum concentration a solution



www.afm-iournal.de

can reach before crystallization becomes a problem. However, the use of multiple salts and asymmetric anions has increased significantly the feasible maximum concentration. [9,12,22] Nevertheless, even in the most concentrated WiS electrolytes, the accumulation of hydrated Li⁺ cations on the negative electrode has constricted approaches to further enhance the reductive stability. [4] Consequently, without elaborate electrode coatings, energy-dense low-potential anode materials such as Li metal or graphite have proven to cycle nonreversibly in WiS electrolytes. Even $\text{Li}_4\text{Ti}_5\text{O}_{12}$ (LTO), which operates at seemingly moderate potentials of 1.55 V versus Li/Li^+ (\approx 1.8 V in concentrated electrolytes [4,7]) lies well below the cathodic stability limit of WiS electrolytes.

Introducing nonaqueous cosolvents into WiS electrolytes is a successful approach to manipulate the interfacial chemistry while increasing the salt concentration with respect to the water fractions, i.e., minimizing, e.g., the ratio of water to Li+. The addition of dimethyl carbonate (DMC) to a concentrated electrolyte based on LiTFSI has enabled stable cycling of ≈3 V LTO/LiNi_{0.5}Mn_{1.5}O₄ cells, mainly due to the contribution of DMC to the formation of an anion- and solvent-derived SEI.^[5] In a similar approach, acetonitrile (AN) was added to aqueous LiTFSI solutions, providing enhanced conductivity, lower viscosity, and a wider temperature range for application in 2.2 V supercapacitors. [23] The combination of AN with more concentrated aqueous LiTFSI solutions also yielded a highly performant electrolyte labelled BSiS-A_{0.5} that allowed for stable cycling of ≈2.3 V LTO/LiMn₂O₄ (LMO) batteries.^[4] In this approach, in addition to anion-derived inorganic SEI layers, the presence of AN contributed to the formation of solvent-derived nitrile-rich outer layers on the SEI.[4] The major drawbacks of such electrolytes comprise the limited salt solubility in organic solvents, as well as their flammability and volatility, which pose risks during the manufacturing process, even though the final electrolyte formulation itself is nonflammable. Capitalizing on the nonflammable and nonvolatile nature of ionic liquids (IL), WiS electrolytes were also combined with ILs such as 1-ethyl-3-methylimidazolium-TFSI (EMImTFSI).^[6] Extremely small water contents in such electrolytes enabled stable cycling of 2.8 V Nb2O5/activated carbon hybrid supercapacitors [24], and another study unraveled the solubility-enhancing effect of EMImTFSI that resulted in threefold enhanced solubility of LiTFSI in the presence of ILs.[7] Such a WiS/IL electrolyte, labelled 40/20-TFSI, is among the most stable aqueous electrolytes reported to date, affording stable cycling of ≈2.3 V LTO/LMO cells as well as ≈2.1 V LTO/ $LiNi_{0.8}Mn_{0.1}Co_{0.1}O_2$ (NMC811) cells.^[7] This is remarkable since NMC811 is known for its incompatibility with water and humid environments, attributed to its complex surface chemistry and reactivity of, particularly de lithiated, NMC811.[25,26] This concept was additionally adapted for sodium-ion batteries, where the achievable salt solubility is often even more limited.^[17] 31m sodium/tetraethylammonium triflate (NaOTf/TEAOTf) and 80m NaTFSI/EMImTFSI electrolytes enabled cycling of 2 V class aqueous sodium-ion batteries with energy densities up to 77 Wh kg⁻¹.[10,17] However, such WiS/IL hybrids, as well as binary salt/IL electrolytes, suffer from low conductivity contributions of the alkali cations, impairing low-temperature and high-rate applications.

In this work, succinonitrile (SN) is introduced to WiS/IL hybrid electrolytes, which leads to a two- to four-fold increase of the ionic conductivity (2-4 mS cm⁻¹) while maintaining outstanding electrochemical stability and performance. Aqueous LTO/NMC811 batteries show excellent cycling stability at 25 and even 0 °C, while also demonstrating strong rate performance for such high-energy aqueous cells, with up to 50% capacity retention at 10C compared to 1C. SN itself is a plastic solid at room temperature, capable of dissolving up to ≈15 mol% of various salts^[27–29] and has a high solubility in water. The combination with its nonvolatile character and polar nitrile groups makes SN a perfect candidate to complement concentrated WiS/IL hybrid electrolytes. Notably, this opens a large design space of quaternary water/ionic liquid/succinonitrile hybrid electrolytes (WISHEs) that can be tailored with respect to maximum electrochemical stability (e.g., minimizing the water content), high rate performance (e.g., increasing the ionic conductivity by cosolvent addition), or minimal cost (e.g., by reducing the salt and/or IL content). By means of Raman and multinuclear NMR spectroscopy as well as molecular dynamics (MD) simulations, the solution structure of two select WISHEs is elucidated and compared to two of the best performing aqueous reference electrolytes, BSiS-A_{0.5} and 40/20-TFSI, while evaluating the achievable electrochemical performance in LTO/NMC811 cells. We highlight the impact of each electrolyte component on the final formulation and show that large fractions of IL decrease the lithium transport number. Rather large SN fractions in quaternary electrolytes, although significantly increasing the ionic conductivity, reduce the electrochemical stability, and, importantly, yield flammable electrolyte formulations. However, WISHEs provide highly competitive electrochemical stability and superior rate capability in energy dense aqueous battery applications if carefully tuned, enabling up to 140 Wh kg⁻¹ on active material level.

2. Results and Discussion

2.1. Physicochemical Properties

Sample composition, conductivity, and flammability of all electrolytes studied here are summarized in Table S1 (Supporting Information), where the numbers, e.g., 1-1-1-1, represent the molar ratio of LiTFSI, EMimTFSI, water, and succinonitrile. We observe significantly improved ionic conductivities with larger fractions of SN and/or IL at a given water-to-salt ratio. Note that we directly aimed for a water-to-salt ratio of 1 or lower (corresponding to >55m of salt per kg of water), in expectation of high electrochemical stability. If the SN fraction exceeds ≈50 mol%, the mixtures become flammable, defeating the purpose of working with aqueous systems. Furthermore, excessive fractions of IL were not considered as this thwarts the potential cost advantage of aqueous electrolytes. Therefore, such electrolytes as well as candidates with ionic conductivities of <2 mS cm⁻¹ were excluded from further investigation. Overall, SN and IL were used to tune the three metrics conductivity versus flammability versus electrochemical stability. Table 1 summarizes the physicochemical properties of the two most promising WISHEs that were studied in more detail: 1-1-1-1,

www.advancedsciencenews.com www.afm-journal.de

Table 1. Physicochemical properties at 25 °C of the four electrolytes studied in detail.

LiTFSI	EMImTFSI	Water	Succinonitrile	Density [g cm ⁻³]	Conductivity [mS cm ⁻¹]	Viscosity [mPa s]	Sample name
1	0.68	1.38	0	1.69	1.2	293	40/20-TFSI ^[7]
1	0	1.11	0 (AN 1.11)	1.57	2.1	76	BSiS-A _{0.5} ^[4]
1	1	1	1	1.55	2.4	102	1-1-1-1 WISHE
1	1	1	2	1.47	4.3	58	1-1-1-2 WISHE

and 1-1-1-2. We also studied two of the best performing aqueous electrolytes from literature that enabled coupling LTO anodes with high-voltage cathodes such as LMO or NMC811: The IL-based LiTFSI₁EMImTFSI_{0.68}water_{1.38} electrolyte (40/20-TFSI^[7]), and the organic solvent-based LiTFSI₁water_{1,11}acetonitrile_{1,11} electrolyte (sample BSiS-A_{0.5}^[4]). Conductivities and viscosities between 0 and 60 °C are shown in Figure S1 in the Supporting Information. 40/20-TFSI is the most viscous (293 mPa s) and least conductive (1.2 mS cm⁻¹) electrolyte in the series, while BSiS-A_{0.5} presents roughly double the ionic conductivity (2.1 mS cm⁻¹) and significantly lower viscosity (76 mPa s). The WISHE 1-1-1-1 has a relatively high conductivity of 2.4 mS cm⁻¹ and low viscosity of 102 mPa s. This is remarkable considering the small water-to-LiTFSI ratio of 1 (molality of 55m), when compared to other electrolytes in the literature that have concentrations of 55.5 m (0.1 mS cm⁻¹, 8555 mPa s)^[12] or 63 m $(0.91 \text{ mS cm}^{-1}, 407 \text{ mPa s})^{[6]}$. Compared to other studies, $^{[6,17]}$ we exclude the IL from the calculation of molality. Although technically a salt, it is considered a cosolvent in these systems. Otherwise, the overall molality in 1-1-1-1 could be stated as 110 m (55 m LiTFSI + 55 m EMImTFSI per kg of water). The increased fraction of SN in 1-1-1-2 significantly increases the ionic conductivity above 4 mS cm⁻¹ and similarly reduces the viscosity. Additionally, both WISHEs have a lower density compared to the reference electrolytes, which is desirable to improve the gravimetric energy density of a cell.

Differential scanning calorimetry (DSC) scans do not show any crystallization upon cooling, or melting upon heating, except for the 40/20-TFSI electrolyte that has a liquidus temperature, the point where it converts into a fully liquid state, of ~15 °C (Figure S2, Supporting Information). DSC further shows that all four electrolytes go through a glass transition below ~–70 to –80 °C, which is typical for such highly concentrated electrolytes. [9] The WISHES and

BSiS- $A_{0.5}$ remained liquid at -18 °C over three months, highlighting the effectiveness of the hybrid solvent approach in resolving concerns about low temperature performance of concentrated electrolytes.

2.2. Structure

To elucidate the impact of each component on the electrolyte performance, solution structures were investigated via Raman and multinuclear NMR spectroscopy as well as molecular dynamics (MD) simulations. Figure 1 shows Raman spectra of the four electrolytes listed in Table 1. The spectra in the wavenumber region corresponding to the O-H stretching vibrations of water molecules (Figure 1a) exhibit a sharp band at ≈ 3550 cm⁻¹, which, compared to the broad signal in pure water, is characteristic for the disrupted hydrogen-bonding network due to strong Li⁺-water interaction in highly concentrated electrolytes.[1,2,30] MD simulations predict that in both 1-1-1-1 and 1-1-1-2 electrolytes O_{water} is coordinated only by 0.06 H_{water} within 2.5 Å (first coordination shell), indicating a largely disrupted hydrogen-bonding network. Compared to the archetypal WiS electrolyte 21m LiTFSI, a redshift of ≈10 wavenumbers is observed for BSiS-A_{0.5} and 40/20-TFSI (peak positions are indicated in Figure 1a). The WISHEs show additional redshifts of 10-20 wavenumbers, reflecting that in all hybrid electrolytes the lithium-water interaction or disruption of the hydrogenbonding network is slightly less pronounced than in binary water-LiTFSI electrolytes. Nitrile groups and/or TFSI from the IL competing with water for a place in the corresponding lithium cation solvation shell could explain this observation, i.e., if more succinonitrile or TFSI is present, the likelihood of some water being displaced from the cation solvation shell increases. This is clearly seen in Figure S3a in the Supporting

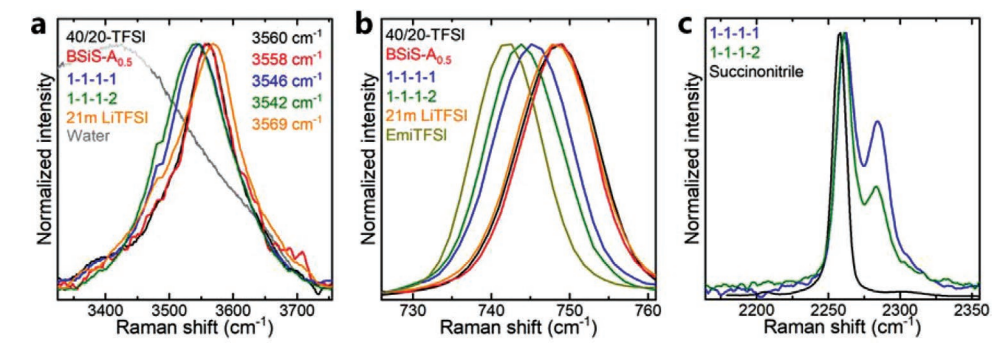


Figure 1. Normalized Raman spectra in the wavenumber region corresponding to the a) O-H stretching vibrations of water, b) the (S-N-S) breathing mode of TFSI, and c) the C \equiv N stretching mode of succinonitrile for the two WISHEs (1-1-1-1 and 1-1-1-2) and the references 40/20-TFSI, BSiS-A_{0.5}, and 21m LiTFSI. In (a) a fraction of the broad signal of pure water is shown for comparison.



www.afm-journal.de

Information, where at a fixed Li⁺-to-water ratio, the addition of more SN leads to an increasing redshift, and in Figure S3b in the Supporting Information, where a similar shift is observed when IL is added as a solvent to 1-0-1-1 or 1-0-1-2. The displacement of water by anions from the IL is thought to be partly responsible for the hydrotropic, i.e., solubility-enhancing, effect of EMImTFSI in water-LiTFSI mixtures.^[7]

Figure 1b shows Raman spectra in the wavenumber region corresponding to the TFSI anions' breathing mode at ≈740–750 cm⁻¹, which is highly sensitive to the coordination environment of the anion. [1,2,31] Typically in concentrated electrolytes a blueshift of this band corresponds to enhanced Li+-TFSI coordination.[1,2,30] The band is observed at lowest wavenumbers in pure EMImTFSI (742 cm⁻¹), indicative of weakest cation-TFSI interactions among the studied electrolytes (i.e., TFSI anions only weakly interact with EMIm via hydrogen bonds and Coulomb interactions). 21m LiTFSI, BSiS-A_{0.5} and 40/20-TFSI show the strongest blueshift (≈748 cm⁻¹), in agreement with comparable, strong Li+-TFSI interactions for the three electrolytes. The 3-5 cm⁻¹ redshift in the WISHEs compared to, e.g., 21m LiTFSI suggests that the Li+-TFSI interaction is less pronounced, again rationalized by the presence of SN as a coordination competitor that makes it more difficult for TFSI to reach the Li+ cation. Figure S4 in the Supporting Information supports this argument, where a redshift for samples with higher SN fractions in binary LiTFSI-SN systems (Figure S4a, Supporting Information) and a redshift with more SN at a fixed Li+-to-water ratio is observed (Figure S4b, Supporting Information). Comparison of Figure S4a and S4b in the Supporting Information further shows that the addition of water causes a redshift. Here, water is the coordination competitor, displacing TFSI from the Li⁺-solvation shell. Adding IL at fixed Li+-to-water-to-SN ratios again results in a redshift (Figure S4c, Supporting Information), which corresponds to the mixture being practically diluted (on average weaker Li⁺-TFSI interaction) by the addition of extra IL solvent and decreasing the Li:TFSI ratio. Reducing the amount of water and IL at a fixed Li⁺-to-SN ratio supports this picture as corroborated by a blueshift at smaller solvent fractions (Figure S4d, Supporting Information). In BSiS-A_{0.5} no redshift compared to 21m LiTFSI is observed due to the presence of AN. It appears that this is related to AN only having one nitrile group and being much smaller than SN, so that both AN and TFSI can tightly coordinate Li⁺ in BSiS-A_{0.5}, i.e., the 1.11 water molecules and 1.11 TFSI anions per cation can fit into the Li+-solvation shell without steric hindrance. On the other hand, the larger SN molecule likely displaces more water and/or TFSI from the Li⁺-solvation shell, leading to the observed redshift in Figure 1b.

Figure 1c shows the Raman spectra of the nitrile $C\equiv N$ stretching mode range where the single peak of SN (\approx 2258 cm⁻¹) is split into two signals in presence of LiTFSI salt (see also Figure S5a in the Supporting Information). The peak at higher wavenumbers (\approx 2284 cm⁻¹) corresponds to SN coordinated to a lithium cation, see Figure S6 in the Supporting Information for more detail. (Comparing the two WISHEs, a lesser amount of coordinated nitrile groups occur with higher fractions of SN in the mixture. Assuming comparable Raman activities for both the coordinated and "free" state (S2), the fraction of coordinated nitrile groups was evaluated to be 28% in 1-1-1-2 and 54% in

1-1-1-1 by fitting two Gaussians to the normalized curves shown in Figure 1c. This means that in 1-1-1-2 most SN is uncoordinated. Given the Li⁺-to-nitrile group ratio of 1:4, however, the 28% indicate that each lithium is coordinated by 1.1 nitrile groups (percentage of coordinated nitriles multiplied by nitrile groups per lithium). Similarly, Li+ coordinates to 1.1 nitriles in 1-1-1-1. The observation that in 1-1-1-1 there is only one SN per Li⁺, but every Li⁺ coordinates to more than one nitrile group, suggests that either some SN molecules coordinate Li+ with both nitriles in a gauche conformation, or that some Li⁺-SN-Li⁺ bridges between two Li+ must have formed. Despite the trans SN conformer being the lowest energy conformer in the gasphase by 3 kJ mol⁻¹ (Figure S7a, Supporting Information), polar gauche conformers are stabilized in the condensed phase (77%[33] in plastic crystals at room temperature, 89% in liquid SN at 60 °C from MD simulations, see Figure S7b in the Supporting Information). MD simulations support the Li⁺-SN-Li⁺ bridging hypothesis with gauche being the dominant conformer as shown in Figures S7 and S8 in the Supporting Information. In 1-1-1-2, Li⁺ is also coordinated by more than one nitrile group, and since there are two SN molecules per Li⁺, it is also possible that two different SN molecules coordinate one Li+ with one nitrile group each. Note that MD predicts 46% of nitrile groups to coordinate Li⁺ in 1-1-1-1 (vs 54% based on Raman) and 38% in 1-1-1-2 (vs 28%). The discrepancy is likely related to the assumption of similar Raman activities in the experimental work, whereas DFT calculations suggest conformer and coordination dependent Raman activities (Figure S6, Supporting Information). Figure S5a,b in the Supporting Information systematically shows increasing fractions of "free" SN with more SN in binary and ternary systems. In accordance with Figure S4 in the Supporting Information, Figure S5c,d in the Supporting Information shows that adding IL or increasing the water and IL fraction releases SN, again driven by the coordination competition between water, TFSI, and SN. In agreement with reference 4, Figure S9 in the Supporting Information supports our interpretation of the Raman data and shows that in BSiS-A_{0.5} also AN coordinates Li⁺ with its nitrile group.

Multinuclear NMR experiments were conducted to further characterize the electrolytes. Figure 2a shows the ¹H NMR chemical shifts of the water hydrogens. In pure water, the extended hydrogen-bonding network results in a high NMR chemical shift of 4.65 ppm.^[19,34] In agreement with the narrow Raman bands shown in Figure 1a, the shielding of ¹H nuclei in concentrated electrolytes corresponds to a rather disrupted hydrogenbonding network, resulting in higher electron density at the water hydrogen atoms (and thus increased shielding).[1,2,19,34] For 40/20-TFSI, the highest shielding and thus presumably the most disrupted hydrogen-bonding network was observed, followed by 21m LiTFSI. Reduced shielding of the water ¹H nuclei is observed for the nitrile containing WISHEs and BSiS-A_{0.5}, highlighting that water forms more hydrogen bonds, i.e., with nitrile groups close by in the Li+ solvation shells. The marginally higher shift of 1-1-1-2 compared to 1-1-1-1 is rationalized by more SN competing with water for coordinating the lithium cations. Additionally, more nitrile groups mean more possible hydrogen bond acceptors available for water.

A common probe to characterize the strength of Li⁺-water interactions is ¹⁷O NMR, which provides characteristic ¹⁷O

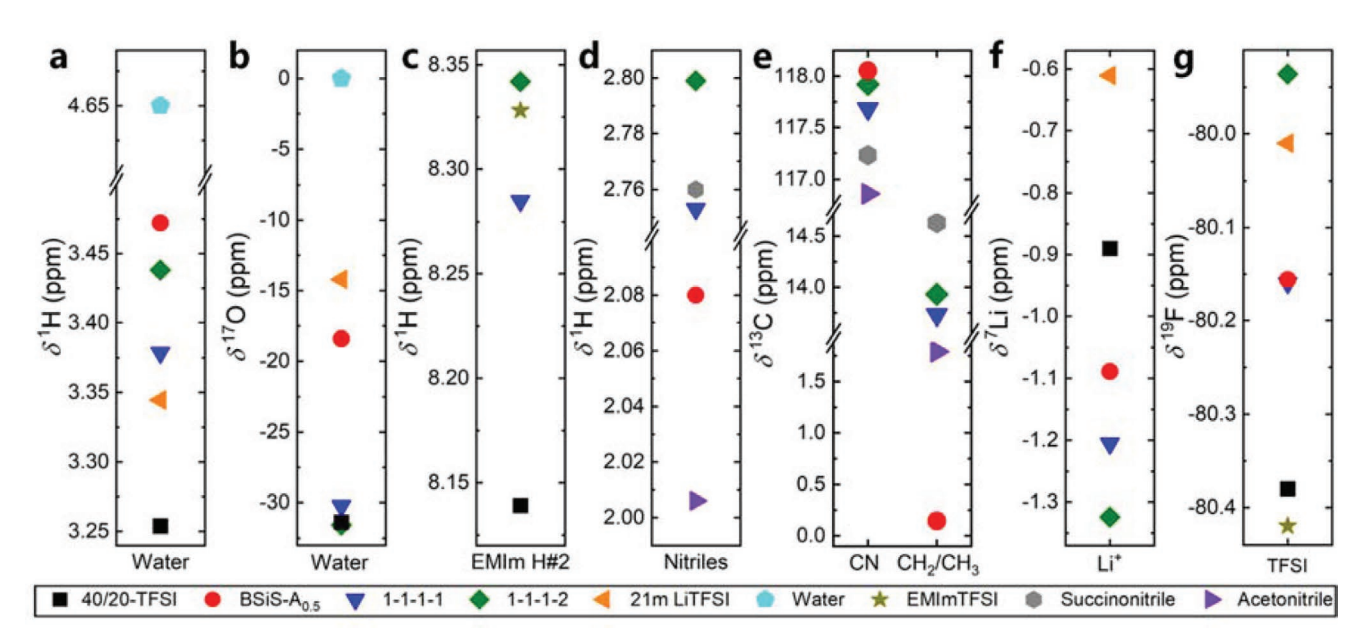


Figure 2. Variations of NMR chemical shifts depending on electrolyte composition: a) $\delta^{1}H$ and b) $\delta^{7}O$ of water, c) $\delta^{1}H$ of EMIm (position 2, structure shown in Figure S11 in the Supporting Information), d) $\delta^{1}H$ of aceto- (CH₃) and succinonitrile (CH₂), e) $\delta^{13}C$ of nitrile and CH₂ or CH₃ carbons of aceto- or succinonitrile, f) $\delta^{1}L$ i, and g) $\delta^{19}F$ of TFS1.

NMR chemical shifts of the water resonance. With increasing LiTFSI concentration, shielding of the ¹⁷O nuclei is observed along with a considerable line broadening, in agreement with a disruption of the water H-bond network discussed above. Figure 2b exhibits ¹⁷O NMR resonances at -13.3 ppm for 21m LiTFSI, -18.4 ppm for BSiS-A_{0.5}, and much more shifted signals at ca. -30 ppm for the IL-containing electrolytes. However, as the observable ¹⁷O NMR chemical shifts of water are dominated by hydrogen bonding^[35], the observed trend in shielding does not exclusively translate to stronger water-Li⁺ coordination, but also attributes to significantly decreased hydrogen bonding to the water oxygen atoms.^[36] Consequently it remains challenging to unambiguously determine the (absolute) strength of the Li⁺-water interactions based on ¹⁷O NMR data, but the large shielding effects perfectly match the redshifts observed in the Raman spectra (Figure 1a), as well as the higher chemical shift in ¹H NMR (Figure 2a), thereby revealing that the water oxygen indeed primarily interacts with Li+ while its hydrogens are pointing away from the cation where various hydrogen bonding partners such as TFSI and nitriles are abundant. This interpretation is further corroborated by a recent study of LiClO₄ in AN/water mixtures showing that water coordinates much more strongly to Li⁺ than nitrile, consistent with the donor numbers of water (33) and AN (14) (15 for SN).[27,37]

Figure 2c displays the ¹H NMR chemical shifts of the EMIm H#2 hydrogen, which is most susceptible to hydrogen bonding with surrounding molecules.^[38,39] The complete spectra and NMR chemical shifts of the other hydrogens, and the chemical structure of EMIm, are shown in Figures S10 and S11 in the Supporting Information. In pure EMImTFSI, the anion is strongly interacting with cations, and in 40/20-TFSI this strong interaction is broken resulting in a lower chemical shift.^[7] Also in case of 1-1-1-1, the ¹H NMR spectrum suggests a reduced amount of hydrogen bonding to EMIm. The higher shift in

1-1-1-2 than in pure EMImTFSI is indicative of stronger hydrogen bonding to the IL cation, which in turn demonstrates that (uncoordinated) SN can also form hydrogen bonds with EMIm.

The ¹H NMR chemical shifts of the SN hydrogens are collected in Figure 2d. The slight deshielding of H#2 in 1-1-1-1 compared to pure SN hints at the following picture: The coordination of SN to Li+ pulls electron density towards the nitrile nitrogen, thus de shielding the nitrile carbon, in turn resulting in shorter C-H bonds and higher electron density (i.e., shielding) of the SN hydrogens. [40] The de shielding of the nitrile carbon upon Li+-SN interaction is documented in the corresponding 13C NMR spectra (Figure 2e, discussed below), where a higher chemical shift is observed in case of 1-1-1-1 compared to pure SN. This is in agreement with a study on valeronitrile-LiFSI mixtures, where higher salt concentration and thus more Li+-nitrile coordination resulted in shielding of ¹H (valeronitrile hydrogens) and de shielding of ¹³C (nitrile carbon) NMR resonances. [40] As the resonances of coordinated and "free" nitrile groups should be slightly different, one could expect to observe two different (¹H and ¹³C) NMR signals when only one nitrile group coordinates to Li+, while if none or both nitriles coordinate, merely a single peak should be observed, as in this case the aliphatic CH₂ groups would be equivalent. However, the solvent exchange rate between the Li⁺ solvation sheath and solution bulk often is too fast with respect to the NMR timescale to resolve the different states, yielding an averaging of the signals, hence one peak only.[37,41,42] The higher SN ¹H NMR chemical shift (Figure 2d) in 1-1-1-2 with a large fraction of uncoordinated SN suggests that SN interacts less with lithium in this WISHE. However, as seen from the ¹³C NMR chemical shifts discussed below, this is not the case and the observed de shielding of ¹H resonances is more likely caused by hydrogen bonding with other molecules within the mixture.

www.afm-journal.de

This fits the high ¹H shifts of EMIm H#2 (Figure 2c) and water hydrogens (Figure 2a) in this WISHE.

Figure 2e exhibits the ¹³C NMR chemical shifts corresponding to the nitrile- and aliphatic carbons of SN and AN. For the nitrile carbons, the shift is lowest for pure AN and SN. Dipole-dipole interactions, and in the salt containing electrolytes particularly ion-dipole interactions (e.g., Li+-nitrile coordination), transfer a significant amount of electron density from the nitrile carbon to the nitrogen, resulting in a higher chemical shift (see again discussion on ¹H NMR chemical shifts in Figure 2d above). [40] BSiS-A_{0.5} shows the highest shift, reflecting strongest Li+-nitrile interaction, in agreement with strong Li⁺-AN coordination described in reference 4 and Figure S9 in the Supporting Information. The lower shift in the WISHEs suggests weaker Li⁺-nitrile interactions, which is plausible i) due to the larger size of SN compared to AN and ii) the presence of more TFSI (from the IL) that competes for a place in the Li⁺ solvation shell. 1-1-1-2 shows a higher ¹³C shift for the nitrile carbon than 1-1-1-1, which fits the slightly larger amount of coordinating nitrile groups per Li⁺ in the former (Figure 1c). With a larger fraction of SN in the mixture, more TFSI is displaced from the Li⁺-solvation shell (Figure 1b) and consequently the Li⁺-nitrile interaction is more likely. The lower ¹³C shifts of the aliphatic carbons in the salt containing electrolytes compared to the pure nitriles again fit the previously described picture (Figure 2d) where Li+-nitrile coordination results in de shielding of the nitrile carbon and shielding of the aliphatic carbons.^[40] The high ¹H shift in BSiS-A_{0.5} (Figure 2d), high ¹³C shift for the nitrile carbon, and low ¹³C shift of the aliphatic carbon compared to pure AN (Figure 2e) again fits the strong Li⁺-AN interaction, as described in reference [4].

⁷Li NMR chemical shifts, shown in Figure 2f, indicate increasing shielding, i.e., higher electron density around the lithium cation, in the order 21m LiTFSI<40/20-TFSI<BSiS-A_{0.5} < 1-1-1-1 < 1-1-1-2. The shielding observed with increasing fractions of coordinating solutes (compare, e.g., 21m LiTFSI with 40/20-TFSI) can be explained by more pronounced incorporation of anions into the solvation shell of Li⁺,[1,7,19] whereas for BSiS-A_{0.5} and the WISHEs coordination of the nitrile lone pairs to Li⁺ additionally promotes this trend.^[24] The higher ⁷Li NMR chemical shift of 1-1-1-1 compared to 1-1-1-2 illustrates even more Li+-SN interaction and/or weaker solvation of Li+ in the former electrolyte. Intuitively this contradicts the ≈50% lower ionic conductivity, as weaker coordination should enable more straightforward movement of Li+. This apparent discrepancy between ⁷Li chemical shift and the observed ionic conductivity may be attributed to differences in Li⁺ transport properties as discussed further below.

Figure 2g shows the ¹⁹F NMR chemical shifts describing the coordination environment of the TFSI anions. In aqueous LiTFSI solutions it was shown that lower ¹⁹F shifts are observed with increasing salt concentration going from –79.2 in 1m LiTFSI to –80.0 ppm in 20m LiTFSI.^[19] This shift is ascribed to stronger anion-anion interactions in more concentrated solutions.^[19] Neat EMImTFSI shows the lowest shift suggesting the strongest TFSI-TFSI interactions. 40/20-TFSI shows a similar shift, in line with the much higher TFSI concentration when compared to 21m LiTFSI. The addition of nitriles, which coordinate lithium, reduces the probability for TFSI to interact with

each other, even at the very high concentrations in BSiS- $A_{0.5}$ and the WISHEs, leading to relatively high chemical shifts comparable to much less concentrated 21m LiTFSI. Comparing 1-1-1-1 with 1-1-1-2 for example shows that SN, in the sense of TFSI-TFSI interactions, dilutes the electrolyte, resulting in the higher 19 F chemical shift.

The self-diffusivities of ⁷Li, ¹⁹F, and ¹H were measured by pulsed field gradient nuclear magnetic resonance (PFG-NMR), accounting for random movement of Li+, TFSI, water, EMIm, or the nitriles, respectively. A comparison of self-diffusion coefficients is shown in Figure S12a in the Supporting Information (see Tables S2-S4 in the Supporting Information for peak assignment, for EMIm the average of all proton signals was used). As anticipated, water has the highest diffusivity in all electrolytes followed by the nitriles, and the overall selfdiffusion decreases with higher viscosity (Table 1). Comparison of the WISHEs shows that the mobility of all components increases upon addition of more SN, in agreement with our analysis above that indicates displacement of TFSI and, to a lesser degree, of water from Li+-solvation shells and in that sense dilution by more SN. In the IL-containing electrolytes the EMIm cation is the most diffusive of the ionic species. Since the trend in diffusivity does not correspond to the degree of hydrogen bonding and IL dissociation as judged by the ¹H chemical shifts in Figure 2c, we suspect that the high diffusivity is rather related to EMIm not being incorporated in the Li⁺-solvation shell, in agreement with the previous discussion.

Interestingly, in BSiS-A_{0.5} the self-diffusivities of water, Li⁺, and the nitrile are higher than in 1-1-1-1, while D_{TESI} is only marginally smaller. This fits the lower viscosity (76 vs 102 mPa s), yet the ionic conductivity (2.1 mS cm⁻¹) is lower than in 1-1-1-1 (2.4 mS cm⁻¹). In the absence of electric fields, PFG-NMR cannot differentiate between unpaired and aggregated entities or ions. Since neutral ion pairs and other aggregates contribute to the determined self-diffusivities but not to the effective ionic conductivity, this suggests that BSiS-A_{0.5} comprises more such neutral ion pairs and aggregates than 1-1-1-1. The quotient of σ_{AC} and σ_{NMR} , the so-called ionicity, can be qualitatively employed to approximate the degree of aggregation, [43,44] where a value close to unity indicates complete dissociation of the salts and the absence of pair/aggregate formation. $\sigma_{
m NMR}$ is calculated from the Nernst-Einstein relation, which connects the selfdiffusion coefficients of spherical moieties such as solvated ions with ionic conductivity under the assumption of uncorrelated motion and that no neutral species are formed (see Table S5 in the Supporting Information)^[45]

$$\sigma_{NMR} = \frac{F^2 \sum cx_i D_i^{NMR}}{RT} \tag{1}$$

where F is the Faraday constant, c is the molar salt concentration that we calculated from the density, x_i is the fraction of ion i, R is the gas constant, T is the absolute temperature, and D_i^{NMR} are the self-diffusion coefficients of the cations and anion as determined by PFG-NMR.

Indeed, we observe higher ionicity, in brackets, suggesting fewer neutral agglomerates in case of 1-1-1-1 (0.6) compared to BSiS- $A_{0.5}$ (0.5). Not surprisingly, 40/20-TFSI (0.2) appears to have the largest fraction of undissociated ion pairs and higher



aggregates in agreement with the observation that TFSI is most strongly incorporated into the Li⁺-solvation shell in this electrolyte (Figures 1 and 2). In fact, the strong incorporation of TFSI into the Li-solvation shell may also explain the low ionicity of BSiS-A_{0.5}. Consequently, the WISHEs, where SN partially replaces TFSI in proximity of Li⁺, have higher apparent degrees of dissociation. This effect is more pronounced with more SN in the mixture (0.7 for 1-1-1-2). The ionicities below unity also agree with the classical Walden rule, as the ratios of molar conductivity and fluidity (inverse viscosity) lie below the ideal KCl line for all electrolytes, see Figure S13 in the Supporting Information for a Walden plot. [46,47] Note that deviations from the Nernst-Einstein relation cannot exclusively be ascribed to permanent association of ions of opposite charge but also the viscosity is a strong factor affecting such deviations. [44]

Based on the self diffusivities we also derived the apparent transference numbers, shown in Figure S12b in the Supporting Information. t_{Li} is lower in the IL-containing electrolytes than in less concentrated WiS electrolytes (\approx 0.6–0.7), [1-3] reflecting that Li⁺ no longer constitutes the major cationic species but rather has a competitor in the form of more mobile EMIm. Accordingly, the larger fraction of IL in the WISHEs affords lower t_{Li} and larger t_{EMIm} values as the competition grows.^[6] This fits the marginally larger $t_{\rm Li}$ and smaller $t_{\rm EMIm}$ in 1-1-1-2 where the IL fraction is only 20 mol%, compared to 25 mol% in 1-1-1-1 (17.3 mol% in 40/20-TFSI). The trend in $t_{\rm TFSI}$ corresponds well to the Raman data shown in Figure 1b that hints at weaker Li-TFSI interactions and thus increased anion mobility in the order 40/20-TFSI < BSiS-A_{0.5} < 1-1-1-1 < 1-1-1-2. The t_{Li} of ≈0.4 in 40/20-TFSI is comparable to $t_{\rm Li}$ in typical organic electrolytes.^[13] The addition of SN further seems to decrease t_{Li} , which is partly compensated by an increased overall ionic conductivity. Multiplying t_{Li} with the ionic conductivities yields apparent lithium conductivities of 0.5 mS cm⁻¹ for 40/20-TFSI, 1.3 mS cm⁻¹ for BSiS-A_{0.5}, 0.6 mS cm⁻¹ for 1-1-1-1, and 1.1 mS cm⁻¹ for 1-1-1-2, respectively. Interestingly, the rate performance of the batteries shown further below does not correspond to this trend of apparent Li⁺ conductivity. This discrepancy can likely be related to different modes of Li⁺ transport and interfacial resistances of the two WISHEs with the electrode materials.

In summary, the spectroscopic analysis reveals strong Li⁺-water and Li⁺-TFSI interactions for all considered electrolytes, suggesting high electrochemical stability due to large overpotentials for water oxidation (strong Li⁺-water interaction)^[1,2] and favorable environments for anion-derived SEI formation (strong Li⁺-TFSI interaction).^[1,2,15] Furthermore, the strong Li⁺-nitrile interactions within the WISHEs do not negatively affect the solution structures, provided that ratios of WISHEs are carefully selected, but rather supplement the available toolbox for tuning hybrid aqueous electrolytes.

2.3. Molecular Dynamics Simulations

MD simulations of WISHEs provide additional insight into the electrolyte structure and ion transport properties. Radial distribution functions (Figure S14, Supporting Information) show that water has the highest affinity to Li⁺ followed by nitrogen of SN and oxygen of TFSI for both 1-1-1-1 and 1-1-1-2 electrolytes.

Due to strong preference of Li $^+$ to be coordinated by water, Li $^+$ is coordinated by 0.90 and 0.85 waters out of the available 1 water per Li $^+$ for 1-1-1-1 and 1-1-1-2 electrolytes, respectively (see Table S6 in the Supporting Information). Increasing the SN fraction from 1 per Li to 2, increases the number of SN coordinating Li $^+$ from 0.89 (out of 1) to 1.57 (out of 2) and consequently decreases the number of O_{TFSI} coordinating Li $^+$ from 2.82 to 2.15, resulting in a smaller size of ionic aggregates and an increased fraction of "free" Li $^+$ not coordinated by O_{TFSI} from 16% to 22%.

Figure S15 in the Supporting Information shows the most probable Li⁺ solvates in the two WISHEs, where the numbers in brackets correspond to Li+ being coordinated by (x O_{TESI}, y N_{SN}, z O_{water}). For example, the transition from 1-1-1-1 to 1-1-1-2 decreases the fraction of solvent-free Li⁺ that is coordinated only by TFSI oxygens, that is (5,0,0) meaning 5 TFSI oxygens and no SN or water, from 14.6% to 5.4%, while SN-rich solvates such as (2,3,0) and (0,3,1) increase from less than 2% to 7.1% and 3.5%, respectively. Furthermore, with addition of SN to 1-1-1-1 the fraction of Li⁺-(TFSI)₃ branching points in ionic aggregates decreases while the fraction of "free" Li+ and Li+ bound to only one TFSI increases (Figure S16, Supporting Information). Additionally, the fraction of "free" TFSI is higher in 1-1-1-2 versus 1-1-1-1. Smaller ionic aggregates and higher fraction of "free" ions formed in 1-1-1-2 compared to 1-1-1-1 are consistent with a higher degree of ion-uncorrelated motion (ionicity) observed in MD simulations, shown in Figure S17 in the Supporting Information, that is also in excellent agreement with the experimentally measured values (Table S5, Supporting Information). Overall, MD simulations predict conductivity, ion and solvent self-diffusion coefficients, and viscosity in excellent agreement with experiments as shown in Figures S1 and S12a, and S13b in the Supporting Information, while the electrolyte structure from MD simulations is fully consistent with spectroscopic findings discussed above.

Analysis of the Li⁺ residence times near water, SN, and TFSI (Table S7, Supporting Information) shows that in 1-1-1-1 Li+ resides near water and TFSI the longest (14-15 ns). In this time a Li⁺ travels 10 Å on average. Li⁺ exchanges nitrile groups about 4.4 times more frequently than water and TFSI (every 3.2 ns on average) and moves only 4.7 Å during this period, which corresponds to the size of a SN molecule. Thus, Li⁺ motion together with water is largely vehicular as Li⁺ moves ca. 4 sizes of water before exchanging it (10 Å), while the SN solvent exchange and Li⁺ motion together with SN contribute similarly to Li⁺ transport. During one Li-SN residence time (≈3 ns), SN changes its conformation multiple times as its dihedral autocorrelation time is only 0.52 ns. These fast conformation changes of SN appear to facilitate Li+ transport, since Li+ has to exchange SN in the bridging Li⁺-SN-Li⁺ networks shown in Figure S8 in the Supporting Information in order to move. This is exemplified by the higher-than-expected ionic conductivity for such highly concentrated electrolytes and the excellent rate performance of full cells discussed below. The larger fraction of SN in 1-1-1-2 compared to 1-1-1-1 decreases the Li+-Owater, Li+-SN and TFSI residence times by 38%, 52% and 57%, respectively, with the largest decrease observed for Li-TFSI as smaller ion aggregates surrounded by SN become more mobile and coordinate less TFSI. Table S7 in the Supporting Information shows that a Li+ moves a shorter distance with TFSI during one residence

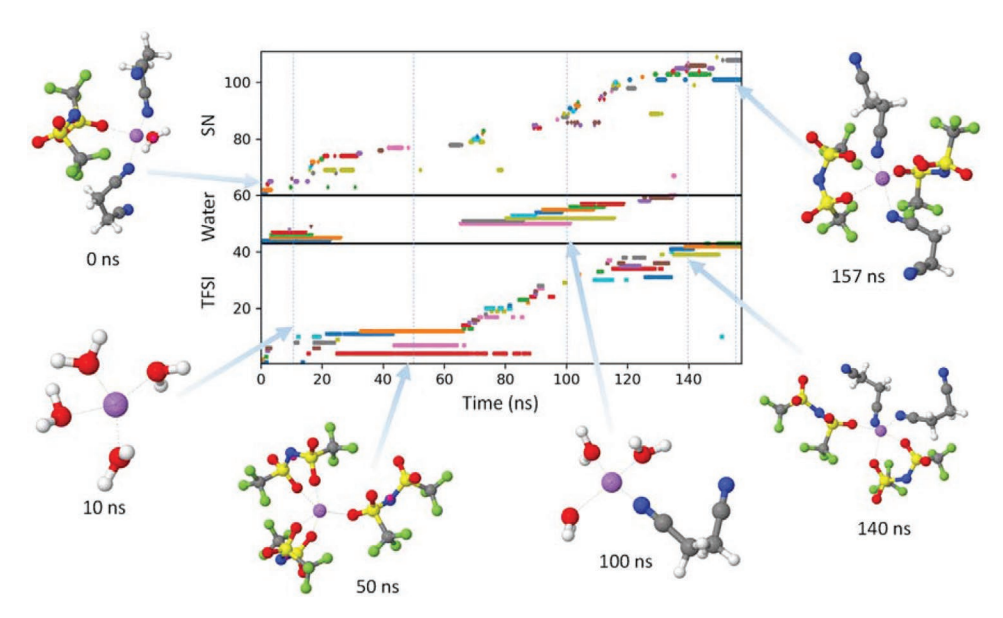


Figure 3. Evolution of the Li⁺ solvation environment in 1-1-1-1 from MD simulations at 25 °C. The top block is for SN, the middle block is for water, and the bottom block is for TFSI. Representative configurations are shown for 0, 10, 50, 100, 140, and 157 ns.

time in 1-1-1-2 versus 1-1-1-1, while it moves a larger distance in one Li-O_{water} residence time, indicating slight changes in the Li⁺ diffusion mechanism. This is consistent with the more pronounced increase of the Li⁺ and TFSI⁻ self-diffusion coefficients than for EMIm cations or water and SN observed in both PFG-NMR experiments and MD simulations.

A detailed picture of the time-dependent Li⁺ solvation environment is shown in Figure 3. If a Li $^{\scriptscriptstyle +}$ is bound to N_{SN} , O_{water} or N_{TFSI} a symbol is placed in the corresponding block versus time. The top block is for SN, middle for water and bottom block for TFSI. This particular lithium cation is initially solvated by water, SN, and TFSI as shown in the snapshot in the top left corner. Over time, the solvation shell is then dominated by water (10 ns), switches to a TFSI rich ionic aggregate (50 ns), changes back to a water dominated environment (100 ns) and eventually mostly consists of TFSI and SN. The numbers on the y-axis allow one to count the number of molecules that are exchanged over the simulation run. In this example, 43 TFSI anions, 17 water molecules, and 49 SN molecules were exchanged for this particular Li⁺. Figure S18 in the Supporting Information shows the evolution of the solvation environment for four additional Li+ cations. From our data it is evident that Li+ is primarily solvated by water and TFSI but often forms short-lived bonds with SN, without breaking the Li-water or Li-TFSI coordination. Thus, stable Li-SN-Li networks as described in binary SN/LiFSI electrolytes do not seem to form.[32] Li hopping as described for such electrolytes is not likely to be a dominant Li-transport mechanism. The short-lived intermittent Li-SN bonds and the fast SN conformation changes however, are likely to contribute to the higher-than-expected Li+ conductivity in WISHEs.

2.4. Electrochemical Performance

The electrochemical stability of electrolytes is commonly evaluated by linear sweep voltammetry, usually on inert electrodes

and with rather high scan rates. The obtained stability windows are often exaggerated when compared to practical stability limits on actual battery electrodes.^[48] Therefore, we conducted cyclic voltammetry at a slow scan rate of 0.1 mV s⁻¹ on activated carbon (AC) electrodes, following the potential opening approach often employed in the supercapacitor community. [49,50] Due to the much larger surface area of AC compared to commonly used, e.g., gold or glassy carbon electrodes and the low scan rate, this test is much more demanding and is more likely to reveal reactions such as anion reduction or water electrolysis without being distorted by excessive overpotentials. In Figure 4 we show the cyclic voltammograms of the studied electrolytes with the last cycle to ±2 V versus Ag/AgCl highlighted as a bold line. For all four electrolytes strong reductive currents are observed between -0.4 and -1 V versus Ag/AgCl, which can be related to TFSI and water reduction, potentially resulting in anion-derived SEI formation.[1,2] Low currents, suggesting electrochemical stability, are observed at lower potentials and an arbitrarily chosen cut-off current of $-5~\mu A~cm^{-2}$ is reached at ≈-1.4 V versus Ag/AgCl for 40/20-TFSI, BSiS-A_{0.5}, and 1-1-1-1, and -1.3 V versus Ag/AgCl for 1-1-1-2. At even more negative potentials, the current density increases again, culminating at a pronounced peak at -2 V versus Ag/AgCl for 40/20-TFSI and BSiS-A_{0.5} that we mostly ascribe to hydrogen formation. Interestingly, this peak is strongly suppressed for 1-1-1-1 and 1-1-1-2, which could be explained by the lower water content of these electrolytes (see again Table 1) and/or formation of a more effective SEI. As discussed below, we conducted X-ray photoelectron spectroscopy (XPS) on electrodes that were cycled in the four electrolytes shown in Figure 4. The results indicate SEI formation in all four electrolytes, which could explain the behavior observed in Figure 4 for the cathodic scans.

On the oxidative side, low currents are measured for all electrolytes and the cut-off of 5 μ A cm⁻² is reached at \approx 1.6 V versus Ag/AgCl for 40/20-TFSI, \approx 1.7 V for BSiS-A_{0.5}, \approx 1.6 V for 1-1-1-1, and \approx 1.3 V for 1-1-1-2. The resulting stability windows

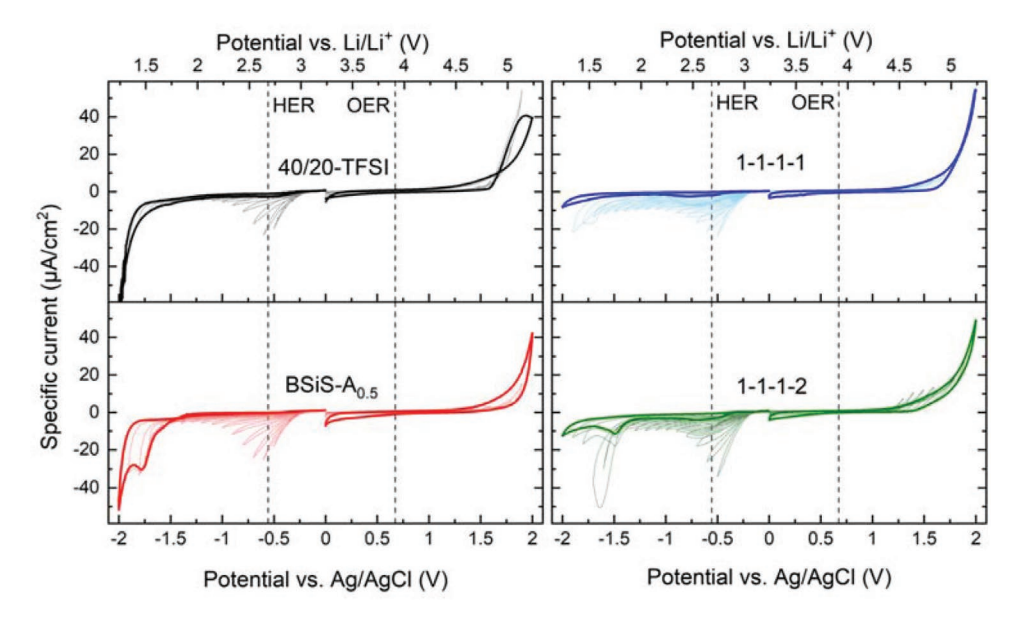


Figure 4. Cyclic voltammograms of 40/20-TFSI, BSiS-A_{0.5}, 1-1-1-1, and 1-1-1-2 over increasing voltage ranges on activated carbon electrodes at a scan rate of 0.1 mV s⁻¹. Anodic and cathodic scans were carried out separately. The specific current is calculated using the geometric area of the electrodes. The dashed vertical lines show the thermodynamic potentials for the hydrogen (HER) and oxygen evolution (OER) reactions at a pH of 6.

of 3 V for 40/20-TFSI and 3.1 V for BSiS-A_{0.5} are significantly lower than the values derived from linear sweep voltammetry on inert electrodes of 4.7 V⁷ and 4.5 V⁴, respectively. However, they correspond much better to the stability of the reported batteries using LTO anodes (≈-1.5 V vs Ag/AgCl in concentrated electrolytes) and LMO or NMC cathodes (≈1.2 V vs Ag/AgCl in concentrated electrolytes). Judged by this experiment the electrochemical stability of the 1-1-1-1 WISHE (3.0 V window) is on par with the best performing reference electrolytes, while 1-1-1-2 is less stable (2.6 V window). The lower stability of the SN rich electrolyte fits our analysis of solution structure, as excess SN results in weaker Li+-water and Li+-TFSI interactions (see again discussions of Raman and NMR data above) which are crucial to enable high electrochemical stability in aqueous electrolytes.

Encouraged by the competitive electrochemical stability of our WISHEs we assembled full cells using LTO and NMC811 electrodes. The cathode material was synthesized in-house via the co-precipitation method and used without any additional coating, while commercial LTO was coated with a NbOx layer by atomic layer deposition. The coating with this fast Li-ion conductor^[51], which shows negligible volume expansion upon Li⁺ intercalation^[52] and low electronic conductivity^[53,54], is a promising way to suppress side reactions like HER as demonstrated in reference 7. In fact, without this coating none of the studied electrolytes performed well unless a significantly oversized cathode was employed (m_{anode} : m_{cathode} ratio of ca. 1:2.5). This includes BSiS-A_{0.5} from reference 4 for which stable operation of LTO was reported. The excess lithium from oversized cathodes can compensate losses on the anode side, e.g., due to electrolyte decomposition and therefore leads to overestimated electrolyte and battery cycling stability, and further reduces the energy density of the cell. Consequently, in our cells we only employed a small excess of cathode material with a Q_{anode}: Q_{cathode} ratio of 1:1.35 (assuming 160 mAh g⁻¹ for LTO and 180 mAh g⁻¹ for NMC811 that is a mass ratio of 1:1.2). The cycling performance at a rate of 1C and the corresponding Coulombic efficiencies (CE) are shown in Figure 5a,b. The cells were cycled between 0.8 and 2.6 V and the rate and capacity are based on the amount of LTO (≈2 mg cm⁻²). All four electrolytes show very stable cycling over the first ≈80–100 cycles with capacities ranging from 145 to 155 mAh g⁻¹ and CEs of up to 99.3% (40/20-TFSI), 99.2% (1-1-1-1), 98.9% (1-1-1-2), and 98.2% (BSiS-A_{0.5}). With initially increasing capacities, 40/20-TFSI and

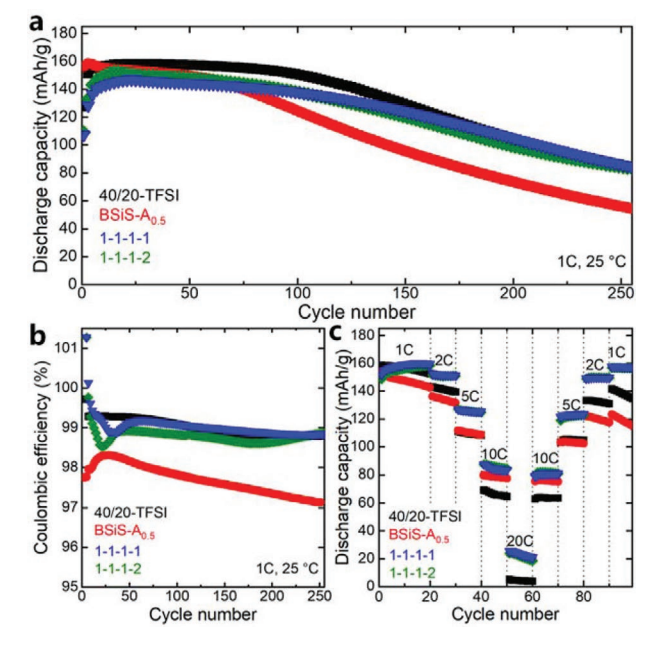


Figure 5. a) Discharge capacity and b) Coulombic efficiency of LTO/ NMC811 cells (mass ratio 1:1.2) cycled between 0.8 and 2.6 V at a rate of 1C (175 mA g^{-1} , \approx 2 mg cm⁻²) at 25 °C in 40/20-TFSI, BSiS-A_{0.5}, and the two WISHEs 1-1-1-1 and 1-1-1-2. c) Rate performance at 1C, 2C, 5C, 10C, and 20C. Capacities and rates are based on anode active material mass.



www.afm-journal.de

the two WISHEs show a pronounced activation over the first 15–25 cycles. In agreement with initially increasing capacities, the WISHE cells further exhibit CEs above 100% for the first cycles. No similar activation is observed in BSiS-A_{0.5}. Storing the cells for 24 or 48 hours before cycling does not influence the duration of the activation period and cycling at lower rates reduces the number of cycles needed before the maximum capacity is reached. This suggests that the activation cannot be explained by incomplete wetting and further understanding of this apparently electrochemical process is subject to ongoing research. Since we do not observe an activation with BSiS-A_{0.5}, we compare the cycle life after the maximum capacity is reached for fairer comparison: 40/20-TFSI reaches 80% of its maximum capacity after 124 cycles from the cycle with said maximum capacity. For the other electrolytes, this threshold is reached after 93 (BSiS-A_{0.5}), 147 (1-1-1-1), and 130 (1-1-1-2) cycles, respectively. After full activation of the electrode materials, the maximum energy densities based on total mass of active materials and average discharge voltages of ≈2.1 V are 145 Wh kg⁻¹ (40/20-TFSI), 150 Wh kg⁻¹ (BSiS-A_{0.5}), 137 Wh kg⁻¹ (1-1-1-1), and 138 Wh kg⁻¹ (1-1-1-2), respectively. In comparison, the cells reach 80% of their initial capacity after 206, 99, 250, and 238 cycles (same sequence of samples). The excellent cycling stability for this demanding cell chemistry for water-containing electrolytes can be in part explained by the formation of an SEI: We conducted XPS on the LTO and NMC811 electrodes after 50 cycles at 1C and found the presence of LiF, Li₂CO₃, and lithium salt residues and the absence of hydroxides on LTO, indicating SEI formation in all four electrolytes (Figures S19-S21, Supporting Information). Furthermore, the XPS results indicate that the LTO and NMC811 active materials remained mostly intact after 50 cycles, suggesting that the capacity fading setting in after 80–100 cycles is mainly due to Li inventory loss. A more detailed discussion of the XPS results can be found in the Supporting Information.

The rate capabilities of the four electrolytes are compared in Figure 5c. The cells for this measurement were identical to the ones above. After 20 cycles at 1C, we conducted 10 cycles each at 2C, 5C, 10C, and 20C, respectively. Except for 1-1-1-2, the rate performance follows the trend in ionic conductivities with the 40/20-TFSI cell losing more capacity at higher rates than with BSiS-A_{0.5} or the two WISHEs. At 10C, the cell with 40/20-TFSI retains 42% of its maximum capacity (measured at 1C), for BSiS-A_{0.5} that is 51%, and 53% for both WISHEs.

What stands out is that 1-1-1-1 outperforms BSiS-A_{0.5} although its apparent lithium conductivity is lower (1.3 mS cm⁻¹ versus 0.6 mS cm⁻¹, see again Figure S12 in the Supporting Information). Additionally, the fact that both WISHEs have the same rate capability, although the ionic conductivity and apparent lithium conductivity of 1-1-1-2 (4.3 and 1.1 mS cm⁻¹, respectively) is almost twice as high as for 1-1-1-1 (2.4 and 0.6 mS cm⁻¹, respectively) is surprising. The better rate performance of the WISHEs compared to the reference electrolytes may in part be explained by the higher ionicity and thus underestimated lithium conductivity in the later, as described before (see again Figure S12a in the Supporting Information): 40/20-TFSI has low apparent σ_{Li} (0.5 mS cm⁻¹) as well as low ionicity (0.2), suggesting poor Li⁺ transport and poor rate performance. BSiS-A_{0.5} has high apparent σ_{Li} (1.3 mS cm⁻¹) but

low ionicity (0.5), which indicates overestimated $\sigma_{l,i}$ that may result in poorer Li+ transport than expected from PFG-NMR. 1-1-1-1 has low apparent σ_{Ii} (0.6 mS cm⁻¹) but high ionicity (0.6), and the good rate performance therefore suggests that the actual t_{Li} is close to the apparent t_{Li} or even higher. It remains unclear why 1-1-1-1 displays as good a rate performance as 1-1-1-2 which has both high apparent σ_{Li} (1.1 mS cm⁻¹) and high ionicity (0.7). It does however fit the ⁷Li chemical shifts that suggest weaker solvation of Li+ and facilitated Li+ transport via fast SN conformation changes in 1-1-1. This indicates that the stronger Li+-SN interactions in 1-1-1-1 than in 1-1-1-2 are beneficial for Li⁺ transport, an important insight for tuning electrolyte component ratios. Note that differences in de solvation/charge transfer kinetics and interfacial resistances at the electrodes may also be partly responsible for this behavior. The WISHEs have generally similar solution/Li+-solvation structures and Li⁺ desolvation or formation of resistive interfaces may be rate limiting, rather than Li⁺ transport in the bulk electrolyte. Post-cycling analysis of anodes and cathodes by XPS, however, did not reveal significant differences in electrodeelectrolyte interphase formation in the two WISHEs (Supporting Information).

In Figure S22a in the Supporting Information we further show rate tests with three times as heavy electrodes (6 mg cm⁻²), observing the same pattern of very similar rate performance for the two WISHEs. Naturally, the rate performance of all electrolytes is worse at higher electrode mass loadings and very little capacity is measured at higher rates than 2C when using the heavier electrodes. Note that the WISHEs yield almost the same capacity at a lower rate of C/2 as with lighter electrodes at 1C. In line with the lower capacity at intermediate to high rates, the Coulombic efficiency improves with the heavier electrodes as less time is spent at high potentials as exemplified for cycling at 1C in Figure S22b,c in the Supporting Information.

As BSiS-A_{0.5} and the two WISHEs did not show any signs of crystallization down to at least -18 °C, we also show a rate test (using again 2 mg cm⁻² electrodes) at 0 °C (Figure S22d, Supporting Information). Not surprisingly, 40/20-TFSI does not provide much capacity even at 1C, likely due to partial crystallization below 15 °C. Interestingly though, BSiS-A_{0.5} shows much better capacity retention at 0 °C than the two WISHEs, and the difference between 1-1-1-1 and 1-1-1-2 is also more pronounced. This does not correspond to the conductivity and viscosity data shown in Figure S1 in the Supporting Information, as also at 0 °C the conductivity increases in the order BSiS- $A_{0.5}$ < 1-1-1-1 < 1-1-1-2, while the opposite trend is observed for the viscosity. This suggests that the solution structure and lithium transfer properties and/or charge transfer kinetics vary significantly between 0 and 25 °C for these electrolytes. However, a more detailed study of this phenomenon is beyond the scope of this work. Rather we conclude that the nitrile containing electrolytes studied here are very well capable of withstanding low temperatures.

3. Conclusions

We studied the solution structure of a new class of water/ ionic liquid/succinonitrile hybrid electrolytes (WISHEs) by means of Raman and multinuclear NMR spectroscopy as well

ADVANCED FUNCTIONAL MATERIALS

as molecular dynamics simulations, and assessed their electrochemical performance. We compare two promising WISHEs with two of the best performing aqueous reference electrolytes and elucidate their coordination structure, transport behavior, and elaborate on the impact of each component on the electrolyte formulation. The highly concentrated WISHEs show better-than-expected ionic conductivity (2-4 mS cm⁻¹) that we explain by reduced ionic aggregation and fewer neutral ion pairs due to Li⁺-succinonitrile interactions. Particularly in the 1-1-1-1 WISHE, strong Li⁺-nitrile coordination facilitates Li+ transport due to fast conformational changes of the succinonitrile molecules and the subsequently highly intermittent solvation environment of Li+. This translates into strong rate performance of aqueous full cells based on Li₄Ti₅O₁₂ and LiNi_{0.8}Mn_{0.1}Co_{0.1}O₂. The WISHEs enable energy dense cells with ≈140 Wh kg⁻¹ of active material with good cycling stability and Coulombic efficiencies close to 99.5% at 1C. Our results further provide guidelines for aqueous hybrid electrolyte development: i) Large fractions of ionic liquid decrease the lithium transport number and are costly, but small amounts improve electrochemical stability and allow for large salt to water ratios, ii) succinonitrile allows for complete circumvention of salt solubility limits in hybrid electrolytes and improves ionic conductivity, but too large fractions render the formulation flammable and decrease the lithium transport number and electrochemical stability due to displacement of water and anions from the lithium solvation shell, iii) intimate Li+-nitrile coordination and fast conformational dynamics of succinonitrile are beneficial for Li⁺ transport, resulting in excellent rate performance. Succinonitrile and potentially other nitriles or solvents with polar functional groups are thus perfect candidates to manipulate solution structures and dynamics of aqueous hybrid electrolytes. Large solvent molecules that can undergo fast conformational changes seem particularly interesting since they may facilitate Li⁺ transport as demonstrated here for succinonitrile.

4. Experimental Section

LiTFSI (99.9%, Solvionic), EMImTFSI (99.9%, Solvionic), succinonitrile (99%, Sigma-Aldrich), and acetonitrile (99.5%, Sigma-Aldrich) were used as received. Electrolytes were prepared by dissolving the components in high-purity water (Millipore Milli-Q) which was previously purged with argon. After preparation, the electrolytes showed a pH value between 6 and 7. pH values were determined using pH paper (Merck) with a pH range from 1 to 14.

lonic conductivity was determined via impedance spectroscopy (Bio-Logic MCS 10) in sealed 2-electrode cells equipped with Pt electrodes (Bio-Logic HTCC). Viscosity was determined with an electromagnetically spinning viscometer (Kyoto Electronics Manufacturing EMS-1000) using 2 mm Al spheres. Sample volumes of 400 μ L were used. The samples were equilibrated for 15 min at each temperature. Density at 25 °C was measured with an Anton Paar DMA 4100 M density meter. Flammability was tested by holding a high power butane torch to an electrolyte-soaked glass fiber pad for one second. The samples with flammability "yes" in Table S1 in the Supporting Information ignited and sustained a steady flame. Samples that "extinguish" ignited upon exposure to the open flame but self-extinguished as soon as the torch was removed. Samples with flammability "no" did not ignite even upon continuous exposure to the flame until all electrolyte evaporated/decomposed and the glass fiber pad melted.

Differential scanning calorimetry was carried out with a Netzsch STA 449 F3 simultaneous thermal analyzer. Approximately 40 mg of

electrolyte sample were mixed with 1–2 mg of meso-carbon microbeads acting as crystallization agent and hermetically sealed in Al pans. The samples were equilibrated at 60 °C for 30 min before scanning to –100 °C followed by a scan back to 60 °C. The scan rate for all measurements was set to 1 °C min $^{-1}$.

Raman spectra of electrolytes sealed in 5 mm NMR tubes were collected at room temperature on a Renishaw Ramascope using a 50 mW laser with a wavelength of 633 nm and a resolution of 1 cm⁻¹.

 $^{1}\text{H},\,^{7}\text{Li},\,^{13}\text{C},\,\text{and}\,^{19}\text{F}$ NMR spectra were recorded at 400.2, 155.5, 100.6, and 376.5 MHz using a 5 mm CryoProbe™ Prodigy probe equipped with z-gradient on a Bruker Avance III 400 NMR spectrometer (Bruker Biospin AG, Fällanden, Switzerland). The ¹⁷O NMR data was recorded at 54.3 MHz on a 5 mm BBO probe since the above mentioned hardware is not dedicated for that frequency range. The 1D NMR experiments were performed at 298 K using the Bruker standard pulse programs and parameter sets applying the following pulse angles/pulse lengths/ number of scans/recycle delays: $10^{\circ}/1.0 \,\mu s/8/8.1 \,s$ (^{1}H); $30^{\circ}/5.0 \,\mu s/32/4 \,s$ (7 Li); 30 $^{\circ}$ /10.0 µs/256/5.4 s (13 C); 90 $^{\circ}$ /15.0 µs/up to 160k/0.1 s (17 O); $20^{\circ}/4.4 \,\mu s/16/5.8 \,s$ (^{19}F) ensuring the quantitative recording of NMR data for all nuclei with the exception of ¹³C. Temperature setting was calibrated using a methanol-d₄ standard sample from Bruker applying the method described in reference [55]. Sealed capillaries containing a 50:50 vol/vol mixture of 2,2,3,3-tetrafluoropropanol (TFP) with CDCl₃ were added to each NMR tube and chemical shifts (δ in ppm) were calibrated to the resonances of TFP at 3.91 (1H), 59.71 (13C), and -127.68 (19F). The 7Li NMR chemical shifts were calibrated to an external reference sample with 9.9m LiCl in D_2O , and the ^{17}O NMR data was referenced to an external sample of pure H₂O at 0.00 ppm.

Pulsed field gradient nuclear magnetic resonance (PFG-NMR) spectra were recorded using a BRUKER 4.7 T AVANCE III instrument with a commercially available BRUKER Diff50 probe. Data was acquired with a (doubly tuned 7Li and $^1H/^{19}F$) 5 mm coil at 25 $^{\circ}C$ (\pm 0.2 $^{\circ}C$). To avoid convection induced by temperature gradients, all samples were kept at 25 °C for 1 h prior to starting the measurements. Doped water, a 0.25 mol L^{-1} LiCl in H_2O and a 3 mol L^{-1} KF in H_2O solution were exploited for external calibration of the system based on their well-known self-diffusion coefficients. The gradient strength during 16 gradient steps was optimized between 600 and 2947 G cm⁻¹ in case of each sample. 16 scans per gradient step, a recycle delay of 4 s, a gradient pulse length δ of 1 ms and a diffusion time Δ of 40 ms (7 Li and 19 F) or 20 ms (1 H) were applied. The self-diffusion coefficients D of the species were derived from a stimulated echo sequence (BRUKER 'diffSte') after fitting the overall attenuated signal amplitudes (integration) to the Stejskal-Tanner equations^[56,57], which describe the case of ("free") isotropic diffusion

$$I = I_0 \times exp\left(-D\gamma^2 \delta^2 g^2 \left(\Delta - \frac{\delta}{3}\right)\right)$$
 (2)

with I being the signal intensity, I_0 the initial signal in the absence of a magnetic field gradient and γ the gyromagnetic ratio. Data analysis was performed with BRUKER Topspin 3.5 and BRUKER Dynamics Center 2.5 MD

The molecular dynamics (MD) simulations were performed using a revised many-body polarizable APPLE&P force field that utilizes atomic induced dipoles to describe polarization.[1,58] The simulation cells contained 216 LiTFSI, EMImTFSI, and 216 or 432 SN for 1111 and 1112 electrolytes, respectively. Both systems were equilibrated at 177 °C for 6 ns, followed by 9 ns equilibration at 90 $^{\circ}$ C, and 20 ns and 20–30 ns equilibration at 60 and 25 °C, respectively, in NPT ensemble. Simulations were performed in NVT ensemble using Nose-Hover thermostat and the average box size was obtained at NPT simulations for 150-200 ns. Multiple-timestep integration was employed with a timestep of 0.5 fs for bonded interactions, a timestep of 1.5 fs for all nonbonded interactions within a truncation distance of 8.0 Å and an outer timestep of 3.0 fs for all nonbonded interactions between 8.0 Å and the nonbonded truncation distance of 14 Å. The Ewald summation method was used for the electrostatic interactions between permanent charges with permanent charges or induced dipole moments with $k = 8^3$ vectors. The



www.afm-journal.de

ADVANCED FUNCTIONAL MATERIALS

reciprocal part of Ewald was calculated every 3.0 fs. Induced dipoles were found self-consistently with convergence criteria of 10^{-9} (electron charge * Å)^[2].

 $Ni_{0.8}Co_{0.1}Mn_{0.1}(OH)_2$ was synthesized in a continuously stirring tank reactor (CSTR) under N_2 atmosphere. Initially, 1 L of distilled water was filled in a 3 L CSTR, and then 2 mol L⁻¹ aqueous solutions of NiSO₄, CoSO₄, and MnSO₄ were fed into the CSTR. Meanwhile, NH₃·H₂O and NaOH were fed into the CSTR as chelating and precipitation agents, respectively. The pH (pH = 11.2), stirring speed (500 rpm) and temperature (50 °C) were maintained during co-precipitation. The $Ni_{0.8}Co_{0.1}Mn_{0.1}(OH)_2$ precursor was filtered and washed several times with distilled water, and then dried at 120 °C overnight. LiNi_{0.8}Co_{0.1}Mn_{0.1}O₂ (NMC811) was obtained by mixing the $Ni_{0.8}Co_{0.1}Mn_{0.1}(OH)_2$ precursor with 3 mol% excess of LiOH·H₂O, then pre-heated at 500 °C for 10 h, followed by calcination at 750 °C for 15 h. The whole calcination was carried out in pure O₂ atmosphere.

Activated carbon and LTO (Targray, type LTO-2s, 4-10 μm (D50), ≤8 m² g⁻¹) electrodes were prepared by dispersing the active material with PVdF binder (Arkema Kynar HSV900) and carbon black (IMERYS SUPER C65) in a mass ratio of 8:1:1 in N-methyl-2-pyrrolidone. NMC811 electrodes were prepared with a mass ratio of 94:3:3 using the same binder and conductive additive. The slurry was tape casted using a doctor blade onto Al foil (AC, LTO) or Ti foil (NMC811). The electrodes were dried for 2 h at 120°C in air and subsequently dried at 120 °C over night under oil pump vacuum. The NMC electrodes were pressed at 1 t cm^{-2} for 30 s after punching out electrode discs with a diameter of 12 mm. The total air-exposure time for NMC811 electrodes was minimized to ≈4 h during electrode preparation. LTO electrode sheets were coated with a niobium oxide layer by atomic layer deposition (ALD) at a substrate temperature of 175 °C with argon as carrier gas at a base pressure of 19 Pa in a Fiji G2 system (Veeco Instruments). The precursors were niobium(V)ethoxide (Nb(OEt)₅, Sigma-Aldrich) and water. Nb(OEt)₅ was kept at 160 °C while the water was unheated. The growth rate of the niobium oxide layer was determined by ellipsometry on Si (100) reference substrates, and linear growth was observed with a growth rate of 0.42 Å cycle⁻¹. In total, 16 ALD cycles were applied.

The stability window of the electrolytes was determined in half-cell configuration by cyclic voltammetry with a scan rate of 0.1 mV s $^{-1}$ using Swagelok T-cells with AC electrodes as working electrodes, activated carbon pellets as counter electrodes, and a miniature Ag/AgCl electrode (eDAQ) as reference electrode. After three conditioning cycles between $\pm 0.4~V$ versus Ag/AgCl, the cut-off potential was increased in 100 mV steps to $\pm 2~V$ versus Ag/AgCl while the second vertex potential was fixed at 0 V versus Ag/AgCl. Three cycles were recorded for each potential to reduce the influence of wetting effects. Separate measurements were conducted for the anodic and cathodic scans, respectively.

Two-electrode full cells were assembled using CR2032 stainless steel coin cells with an Al-coated negative cell casing part and a Ti disc with a diameter of 16 mm between positive electrode and spacer disc (1 mm). Whatman GF/D glass microfiber filters with a diameter of 15 mm were used as separators. The electrolyte volume was set to 75 $\mu L.$ All cells were assembled under inert atmosphere in an argon-filled glovebox (MBraun). All cycling data was obtained at 25 °C.

X-ray photoelectron spectroscopy (XPS) measurements were performed on a PHI Quantum 2000 using a monochromated Al K α X-ray source (1486.6 eV) with a pass energy of 30 eV. All measurements were conducted on three different areas, 150 μ m in diameter, of each sample. Sample charging was prevented by charge compensation provided by a low energy electron and an argon ion gun. XPS data were processed with the CasaXPS software and quantified using the corrected cross sections with the instrument parameters (see ref. [17]). Spectra were calibrated by setting the hydrocarbon component of the C1s photoemission peak to 285.0 eV binding energy. A detailed description of the XPS data fitting procedure is given in the Supporting Information. The cycled electrodes were rinsed by dipping them in water three times for two seconds each. A slight stirring motion helped to remove most glass-fiber separator residues that stuck to the electrodes.

Supporting Information

Supporting Information is available from the Wiley Online Library or from the author.

Acknowledgements

The NMR hardware was partially financed by the Swiss National Science Foundation (grant no. 206021_150638/1). The modeling part of this work conducted at ARL was supported by the Joint Center for Energy Storage Research (JCESR), a Department of Energy, Energy Innovation Hub, under cooperative agreement number W911NF-19-2-0046.

Open access funding provided by ETH-Bereich Forschungsanstalten.

Conflict of Interest

The authors declare no conflict of interest.

Data Availability Statement

The data that support the findings of this study are available from the corresponding author upon reasonable request.

Keywords

batteries, ionic liquids, MD simulations, water-in-salt electrolytes

Received: January 18, 2022 Revised: February 2, 2022 Published online: February 27, 2022

- [1] L. Suo, O. Borodin, T. Gao, M. Olguin, J. Ho, X. Fan, C. Luo, C. Wang, K. Xu, Science 2015, 350, 938.
- [2] Y. Yamada, K. Usui, K. Sodeyama, S. Ko, Y. Tateyama, A. Yamada, Nat. Energy 2016, 1, 16129.
- [3] L. Suo, O. Borodin, W. Sun, X. Fan, C. Yang, F. Wang, T. Gao, Z. Ma, M. Schroeder, A. Cresce, S. M. Russell, M. Armand, A. Angell, K. Xu, C. Wang, Angew. Chem., Int. Ed. 2016, 55, 7136.
- [4] J. Chen, J. Vatamanu, L. Xing, O. Borodin, H. Chen, X. Guan, X. Liu, K. Xu, W. Li, Adv. Energy Mater. 2020, 10, 1902654.
- [5] F. Wang, O. Borodin, M. S. Ding, M. Gobet, J. Vatamanu, X. Fan, T. Gao, N. Edison, Y. Liang, W. Sun, S. Greenbaum, K. Xu, C. Wang, *Joule* 2018, 2, 927.
- [6] L. Chen, J. Zhang, Q. Li, J. Vatamanu, X. Ji, T. P. Pollard, C. Cui, S. Hou, J. Chen, C. Yang, L. Ma, M. S. Ding, M. Garaga, S. Greenbaum, H. S. Lee, O. Borodin, K. Xu, C. Wang, ACS Energy Lett. 2020, 5, 968.
- [7] M. Becker, D. Rentsch, D. Reber, A. Aribia, C. Battaglia, R.-S. Kühnel, Angew. Chem., Int. Ed. 2021, 60, 14100.
- [8] R.-S. Kühnel, D. Reber, C. Battaglia, ACS Energy Lett. 2017, 2, 2005.
- [9] D. Reber, R.-S. Kühnel, C. Battaglia, ACS Mater. Lett. 2019, 1, 44.
- [10] L. Jiang, L. Liu, J. Yue, Q. Zhang, A. Zhou, O. Borodin, L. Suo, H. Li, L. Chen, K. Xu, Adv. Mater. 2020, 32, 1904427.
- [11] J. Forero-Saboya, E. Hosseini-Bab-Anari, M. E. Abdelhamid, K. Moth-Poulsen, P. Johansson, J. Phys. Chem. Lett. 2019, 10, 4942.
- [12] S. Ko, Y. Yamada, K. Miyazaki, T. Shimada, E. Watanabe, Y. Tateyama, T. Kamiya, T. Honda, J. Akikusa, A. Yamada, *Electro-chem. Commun.* 2019, 104, 106488.
- [13] O. Borodin, L. Suo, M. Gobet, X. Ren, F. Wang, A. Faraone, J. Peng, M. Olguin, M. Schroeder, M. S. Ding, E. Gobrogge, A. Von Wald

www.advancedsciencenews.com www.afm-journal.de

- Cresce, S. Munoz, J. A. Dura, S. Greenbaum, C. Wang, K. Xu, ACS Nano 2017, 11, 10462.
- [14] K. Miyazaki, N. Takenaka, E. Watanabe, S. Iizuka, Y. Yamada, Y. Tateyama, A. Yamada, J. Phys. Chem. Lett. 2019, 10, 6301.
- [15] L. Suo, D. Oh, Y. Lin, Z. Zhuo, O. Borodin, T. Gao, F. Wang, A. Kushima, Z. Wang, H. C. Kim, Y. Qi, W. Yang, F. Pan, J. Li, K. Xu, C. Wang, J. Am. Chem. Soc. 2017, 139, 18670.
- [16] S. Ko, Y. Yamada, A. Yamada, ACS Appl. Mater. Interfaces 2019, 11, 45554.
- [17] D. Reber, R. Grissa, M. Becker, R.-S. Kühnel, C. Battaglia, Adv. Energy Mater. 2021, 11, 2002913.
- [18] H. G. Steinrück, C. Cao, M. R. Lukatskaya, C. J. Takacs, G. Wan, D. G. Mackanic, Y. Tsao, J. Zhao, B. A. Helms, K. Xu, O. Borodin, J. F. Wishart, M. F. Toney, Angew. Chem., Int. Ed. 2020, 59, 23180.
- [19] N. Dubouis, P. Lemaire, B. Mirvaux, E. Salager, M. Deschamps, A. Grimaud, Energy Environ. Sci. 2018, 11, 3491.
- [20] J. Vatamanu, O. Borodin, J. Phys. Chem. Lett. 2017, 8, 4362.
- [21] M. McEldrew, Z. A. H. Goodwin, A. A. Kornyshev, M. Z. Bazant, J. Phys. Chem. Lett. 2018, 9, 5840.
- [22] M. Becker, R.-S. Kühnel, C. Battaglia, Chem. Commun. 2019, 55, 12032.
- [23] Q. Dou, S. Lei, D. W. Wang, Q. Zhang, D. Xiao, H. Guo, A. Wang, H. Yang, Y. Li, S. Shi, X. Yan, Energy Environ. Sci. 2018, 11, 3212.
- [24] Q. Dou, Y. Wang, A. Wang, M. Ye, R. Hou, Y. Lu, L. Su, S. Shi, H. Zhang, X. Yan, Sci. Bull. 2020, 65, 1812.
- [25] E. M. Erickson, F. Schipper, T. R. Penki, J.-Y. Shin, C. Erk, F.-F. Chesneau, B. Markovsky, D. Aurbach, J. Electrochem. Soc. 2017, 164, A6341.
- [26] M. Gauthier, T. J. Carney, A. Grimaud, L. Giordano, N. Pour, H. H. Chang, D. P. Fenning, S. F. Lux, O. Paschos, C. Bauer, F. Maglia, S. Lupart, P. Lamp, Y. Shao-Horn, J. Phys. Chem. Lett. 2015, 6, 4653.
- [27] P. J. Alarco, Y. Abu-Lebdeh, A. Abouimrane, M. Armand, Nat. Mater. 2004. 3, 476.
- [28] A. Abouimrane, P. S. Whitfield, S. Niketic, I. J. Davidson, J. Power Sources 2007, 174, 883.
- [29] P. S. Whitfield, A. Abouimrane, I. J. Davidson, Solid State Ionics 2010, 181, 740.
- [30] D. Reber, R. Figi, R.-S. Kühnel, C. Battaglia, *Electrochim. Acta* 2019, 321, 134644.
- [31] I. Rey, P. Johansson, J. Lindgren, J. C. Lassègues, J. Grondin, L. Servant, J. Phys. Chem. A 1998, 102, 3249.
- [32] Y. Ugata, M. L. Thomas, T. Mandai, K. Ueno, K. Dokko, M. Watanabe, Phys. Chem. Chem. Phys. 2019, 21, 9759.

- [33] P. Derollez, J. Lefebvre, M. Descamps, W. Press, H. Fontaine, J. Phys. Condens. Matter 1990, 2, 6893.
- [34] K. Mizuno, K. Oda, S. Maeda, Y. Shindo, J. Phys. Chem. 1995, 99, 3056
- [35] K. Mizuno, K. Oda, Y. Shindo, A. Okumura, J. Phys. Chem. 1996, 100, 10310.
- [36] J. Reuben, J. Am. Chem. Soc. 1969, 91, 5725.
- [37] E. Pasgreta, R. Puchta, A. Zahl, R. Van Eldik, Eur. J. Inorg. Chem. 2007, 13, 1815.
- [38] S. Cha, M. Ao, W. Sung, B. Moon, B. Ahlström, P. Johansson, Y. Ouchi, D. Kim, Phys. Chem. Chem. Phys. 2014, 16, 9591.
- [39] A. Yokozeki, D. J. Kasprzak, M. B. Shiflett, Phys. Chem. Chem. Phys. 2007, 9, 5018.
- [40] J. Neuhaus, E. von Harbou, H. Hasse, Polyhedron 2020, 183, 114458.
- [41] X. Bogle, R. Vazquez, S. Greenbaum, A. V. W. Cresce, K. Xu, J. Phys. Chem. Lett. 2013, 4, 1664.
- [42] P. Zuman, Microchem. J. 2003, 75, 139.
- [43] R.-S. Kühnel, A. Balducci, J. Phys. Chem. C 2014, 118, 5742.
- [44] Y. Shao, K. Shigenobu, M. Watanabe, C. Zhang, J. Phys. Chem. B 2020, 124, 4774.
- [45] M. Chintapalli, K. Timachova, K. R. Olson, S. J. Mecham, D. Devaux, J. M. Desimone, N. P. Balsara, *Macromolecules* 2016, 49, 3508.
- [46] M. Yoshizawa, W. Xu, C. A. Angell, J. Am. Chem. Soc. 2003, 125, 15411.
- [47] P. Walden, Z. Phys. Chem. 1906, 55, 207.
- [48] R.-S. Kühnel, D. Reber, C. Battaglia, J. Electrochem. Soc. 2020, 167, 70544
- [49] D. Weingarth, H. Noh, A. Foelske-Schmitz, A. Wokaun, R. Kötz, Electrochim. Acta 2013, 103, 119.
- [50] D. Reber, R.-S. Kühnel, C. Battaglia, Sustainable Energy Fuels 2017, 1, 2155.
- [51] V. Augustyn, J. Come, M. A. Lowe, J. W. Kim, P. L. Taberna, S. H. Tolbert, H. D. Abruña, P. Simon, B. Dunn, *Nat. Mater.* 2013, 12, 518.
- [52] N. Kumagai, Y. Koishikawa, S. Komaba, N. Koshiba, J. Electrochem. Soc. 1999, 146, 3203.
- [53] Q. Deng, Y. Fu, C. Zhu, Y. Yu, Small 2019, 15, 1804884.
- [54] S. Zhu, P. Xu, J. Liu, J. Sun, Electrochim. Acta 2020, 331, 135268.
- [55] M. Findeisen, T. Brand, Magn. Reson. Chem. 2007, 45, 175.
- [56] P. W. Kuchel, G. Pagès, K. Nagashima, S. Velan, V. Vijayaragavan, V. Nagarajan, K. H. Chuang, Concepts Magn. Reson. Part A Bridg. Educ. Res. 2012, 40 A, 205.
- [57] D. Sinnaeve, Concepts Magn. Reson. Part A Bridg. Educ. Res. 2012, 40 A, 39.
- [58] O. Borodin, J. Phys. Chem. B 2009, 113, 11463.